ФИЗИКА ЭЛЕМЕНТАРНЫХ ЧАСТИЦ И АТОМНОГО ЯДРА
2012. Т. 43. ВЫП. 6

STUDY OF THE NEUTRON FLUX GENERATED AT E-LINAC-DRIVEN NEUTRON SOURCES

*G. G. Bunatian**

Joint Institute for Nuclear Research, Russia

*E-mail: bunat@cv.jinr.ru

ФИЗИКА ЭЛЕМЕНТАРНЫХ ЧАСТИЦ И АТОМНОГО ЯДРА
2012. Т. 43. ВЫП. 6

STUDY OF THE NEUTRON FLUX GENERATED AT E-LINAC-DRIVEN NEUTRON SOURCES

*G. G. Bunatian**

Joint Institute for Nuclear Research, Russia

We treat generic physical features of the production of neutrons from the high-atomic-number materials irradiated by the electron beam provided by the linear electron accelerator. The bremsstrahlung of incident electrons inducing the photonuclear reactions is considered. The experimental data on photonuclear reactions are utilized to describe neutrons generating caused by the γ-radiation absorption. The generally received theoretical approaches are applied to explore the photoneutrons energy distribution. The produced neutrons are primarily statistical, yet the direct neutrons share is noteworthy as well. The dependence of the neutron spectrum, mean neutron energy, and total neutron yield on the energy and current of the electron beam and on the characteristics of irradiated samples is investigated. The analysis is plainly carried out in the framework of the quantum electrodynamics and photonuclear physics, without having any recourse to the «numerical Monte-Carlo simulations». Our findings prove mainly to conform satisfactorily to the experimental measurements, so far as those are available for now.

Исследуются основные физические характеристики процесса получения нейтронов посредством облучения потоком электронов материалов с большими атомными номерами. Рассмотрено тормозное излучение электронов, которое производит фотоядерные реакции. Экспериментальные данные, полученные в исследованиях фотоядерных реакций, используются для описания выхода нейтронов при поглощении γ-излучения ядрами. Распределение фотонейтронов по энергиям исследуется на основе существующих теоретических моделей. Нейтроны, статистически распределенные по энергии, составляют основную часть всех получаемых нейтронов, доля прямых нейтронов также учитывается в расчетах. Спектр нейтронов, средняя энергия и полный выход нейтронов вычисляются в зависимости от энергии и тока электронов и от характеристик облучаемых образцов. Исследование выполнено без обращения к «численному моделированию Монте-Карло». Результаты вычислений удовлетворительно согласуются с результатами соответствующих экспериментальных измерений.

PACS: 29.25.Dz; 28.20.Gd

INTRODUCTION

Nowadays, the e-linac-based neutron sources find applications in a variety of fields of science, technology, medicine, etc. These facilities are inherently compact, economical, reliable, easy to handle, less hazardous in nature, and most

*E-mail: bunat@cv.jinr.ru

suitable for applications such as neutron capture and fission cross-section studies, radioisotope production and basic neutron-scattering experiments for material-science studies, etc. [1]. For recent years, the special interest was focused on the investigations with fast, nonmoderated neutrons.

The primary generic performances of considered sources are the total neutron flux and neutron energy distribution, treated in the work presented. Being of general value by itself, the knowledge of neutron spectrum is essential in treating the nuclear reactions $(n, n'\gamma)$, (n, γ), (n, xn), $(n, \mathrm{fission})$, as their cross-sections substantially depend on neutron energy, and the thresholds of these reactions actually constitute $\gtrsim 1$ MeV. Study of these processes in medium is needful to design and construct the fusion reactors, hybrid reactors, transmutation assemblies and, especially, the Accelerator Driven Systems harnessing the energy of nuclear reactions in an uranium bulk. The recent investigations concerning the Reactor Accelerator Coupling Experiments and the Coupling of Subcritical Assembly with neutron sources [2] prove that the e-linac-based neutron sources can serve as a practicable alternative to the spallation neutron sources. Although the process of conversion of an electron beam via bremsstrahlung and photoneutron production is not very efficient in neutron generating as compared to the spallation neutron process, however, the reliability, low cost, compactness and ease of operation make the e-linac-driven neutron sources as a viable alternative. Beyond all questions, these promising explorations require the neutron spectrum to be acquired, that is what our work is aimed at.

Of course, besides the neutron spectra, other aspects are to be considered in planning and performing actual experiments at certain facilities: pulse repetition, pulse length, number of neutrons per burst, heat deposition in radiator and its cooling, radiation safety, etc., which can vary from measurement to measurement. These aspects, though extremely important, call for special treatment, and are beyond the scope of the study presented.

First, we consider in Sec. 1 the absorption of the bremsstrahlung induced by an initial electron beam, which causes the photoneutron production. In Secs. 2 and 3, we analyze the photoneutron production by absorbing γ rays with the energy E_γ within the giant resonance range, Sec. 2, and with E_γ beyond that energy area, Sec. 3. In the last Sec. 4, we discuss the outcome of computations and correlate our findings with the results of other investigations available for now.

1. THE PHOTONEUTRON PRODUCTION BY THE BREMSSTRAHLUNG FLUX

At e-linac-driven neutron sources, neutrons are produced through the photonuclear reactions caused by the bremsstrahlung of electrons interacting with high-Z nuclei of an irradiated sample.

An electron beam, with a given electron energy E_e and current density $J_e(t)$ [A/cm^2] (generally speaking, time-dependent), travels through an irradiated sample (see Fig. 1), that is prepared of a proper heavy element $A_S(Z_S, N_S)$, such as W, U, Pb, Ta, etc. The bremsstrahlung is thereby induced with the current density

$$J_{S\gamma}(E_\gamma) = \frac{\mathcal{N}_\gamma(E_\gamma)}{\mathrm{s}\cdot\mathrm{cm}^2\cdot\mathrm{MeV}}, \qquad (1.1)$$

expressed in terms of the photon number $\mathcal{N}_\gamma(E_\gamma)$ with the energy $E_\gamma{=}|\mathbf{k}|{=}k$, per 1 cm^2, 1 s, 1 MeV. In turn, that γ-ray flux, interacting with nuclei $A_S(N_S, Z_S)$ of the sample (see Fig. 1), induces the photonuclear reactions

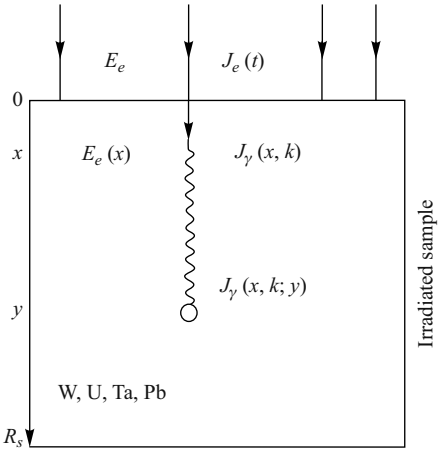

Fig. 1. The scheme of neutron yield by an electron beam

$$\gamma + A_S(Z_S, N_S) \Longrightarrow A'_S(Z_S, N_S - 1) + n, \qquad (1.2)$$

$$\gamma + A_S(Z_S, N_S) \Longrightarrow A'_S(Z_S - 1, N_S - 1) + n + p, \qquad (1.3)$$

$$\gamma + A_S(Z_S, N_S) \Longrightarrow A'_S(Z_S, N_S - 2) + 2n, \qquad (1.4)$$

$$\ldots\ldots,\ldots\ldots\ldots\ldots\ldots\ldots\ldots\ldots\ldots\ldots\ldots$$

$$\gamma + A_S(Z_S, N_S) \Longrightarrow \text{fission fragments} + \nu_{\gamma nF}\ \text{fission neutrons}, \qquad (1.5)$$

where $\nu_{\gamma nF}$ stands for multiplicity of the neutrons accompanying the photofission. Hereinafter, the index S designates the sort of material of irradiated sample, $S = \mathrm{U}, \mathrm{Ta}, \mathrm{Pb}, \ldots$ In the ordinary way, all the evaluations we make in the work are of the lowest α-order, and we abandon contributions from all the high α-order processes. The direct nuclear reactions induced by electrons are left out as well. The direct production of neutrons by electrons is about two orders of magnitude smaller than the neutron production by high-energy photons.

Certainly, the processes (1.2)–(1.5) can only be realized, when the energy E_γ of γ radiation is greater than the neutron binding energy B_n and the fission threshold energy B_F of a considered nucleus $A_S(Z_S, N_S)$, $E_\gamma > B_n, B_F$. Actually, these processes will successfully run provided E_γ is of the order of, and comes over the energy E_{GR} of giant resonance in the photonuclear reactions on respective nuclei, $E_\gamma \gtrsim E_{\mathrm{GR}}(Z, N) \sim 10{-}17$ MeV. As a matter of course, an electron must have got the energy $E_e > E_\gamma$ in order to give birth to the bremsstrahlung with the required energy E_γ. Thus, only the processes

involving the electron and photon energies

$$E_\gamma\,,\; E_e \gtrsim E_{\rm GR} \tag{1.6}$$

are to be taken into consideration and explored, which is the key point of our treatment. Next, we limit the current study by the condition

$$E_e \lesssim 100 \text{ MeV} \tag{1.7}$$

as well. From the very first, it is to emphasize that we perform our calculations plainly in the framework of the quantum electrodynamics and photonuclear physics, without any resort to the widely to-day utilized «numerical Monte-Carlo simulation». The relations (1.6), (1.7) govern all the presented calculations, specifying the energy area where our consideration holds true. Thus, we are not in need of entire description of the electron–photon cascade setup in an irradiated sample, as the particles participating therein would mostly have got energies beyond the key restriction (1.6) (see [3]). Then, upon carrying out the straightforward calculation, we obtain the bremsstrahlung flux at a distance y from the initial edge of sample,

$$J_{S\gamma}(k, E_e, Z_S, \rho_S, t; y) = \\ = J_e(t)\mathcal{N}_S \int\limits_0^y dx \frac{d\sigma_{Sb}(k, E_e(x, E))}{dk} \exp\left(-\frac{y-x}{l_S(Z_S, \mathcal{N}_S, \rho_S, k)}\right). \tag{1.8}$$

Here $\dfrac{d\sigma_{Sb}(k, E_e(x, E))}{dk}$ stands for the cross-section of bremsstrahlung of an electron with the energy $E_e(x, E)$ at a distance x from the starting edge of sample, see [4–8]. The exponent in Eq. (1.8) describes the γ-flux decrease in passing a distance $(y-x)$, see Fig. 1. The γ-ray absorption lengths, $l_S(k)$, are found, for instance, in [4–6,9]. For a given electron initial energy $E_e(0) = E$, the dependence $E_e(x, E)$ was obtained in [3] in terms of the irradiated sample characteristics. In expression (1.8), the number $\mathcal{N}_S$ of scattering atoms of converter in 1 cm^3 is

$$\mathcal{N}_S = \frac{\rho_S \cdot 6.022 \cdot 10^{23}}{A_S}, \tag{1.9}$$

where ρ_S is the density of sample material, and A_S is its atomic weight.

As plain evaluation proves, the quantity $J_{S\gamma}(k, E_e, Z_S, \rho_S, t; y)$ (1.8) firstly increases with y growth, gets its maximum at $y_{\max}(E_e)$, and then falls down, tending to zero. In Fig. 2, we display k dependence of the γ flux (1.8) at the distances $y_{\max}$ at which $J_{S\gamma}(k, E_e, Z_S, \rho_S, t; y)$ gets its maximum for a given initial electron energy $E_e = E_e(0)$.

Our purpose is to explore the energy and angular distribution of the neutron flux caused by the reactions (1.2)–(1.5). We calculate a number of neutrons,

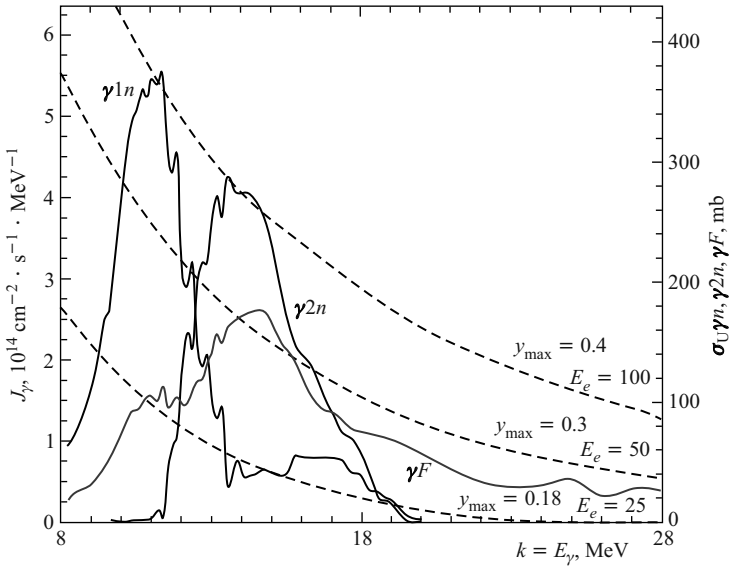

Fig. 2. The dashed curves represent the k-dependence of the γ flux (1.8) $J_{\mathrm{U}\gamma}(k; y)$ at $y = y_{\max}$ (cm), where this quantity $J_{\mathrm{U}\gamma}(k; y)$ gets its maximum for different initial energies E_e (MeV); the initial electron current density $J_e = 1$ mA/cm^2. The values of $y_{\max}$ and E_e are plotted along the corresponding curves. The solid curves represent k-dependence of the uranium photoabsorption cross-sections. The curves tagged by $\boldsymbol{\gamma} 1n$, $\boldsymbol{\gamma} 2n$, $\boldsymbol{\gamma} F$ stand for the $\boldsymbol{\sigma}_{\mathrm{U}}\boldsymbol{\gamma}_{1n}(k)$, $\boldsymbol{\sigma}_{\mathrm{U}}\boldsymbol{\gamma}_{2n}(k)$, $\boldsymbol{\sigma}_{\mathrm{U}}\boldsymbol{\gamma}_F(k)$ cross-sections, respectively

emitted within a solid angle $d\Omega = \sin\theta\, d\theta\, d\varphi$, with a given energy ε, produced per a unit of time, from a homogeneous sample of the longitudinal size R_S (see Fig. 1), irradiated by the γ flux (1.8), that, in turn, is produced by the primary electron beam with the initial energy $E_e(0)$ and current density J_e. For the sample transverse area equal to 1 cm^2, this distribution proves to be written as follows:

$$\Phi_S(\varepsilon, \theta, E_e(0), J_e, R_S; t) = \frac{d^2 n_S(\varepsilon, \theta, E_e(0), J_e, R_S; t)}{d\varepsilon\, d\Omega} =$$

$$= \mathcal{N}_S \int_0^{R_S} dy \int_0^{\infty} dk\, J_{S\gamma}(k, E_e, Z_S, \rho_S, t; y) \times$$

$$\times \left(\sum_{j=1,2,\ldots} j\sigma_{S\gamma jn}(k) \frac{d^2 n_{S\gamma jn}(k, \varepsilon, \theta)}{d\varepsilon\, d\Omega} + \sigma_{S\gamma F}(k) \nu_{S\gamma nF}(k) \frac{d^2 n_{S\gamma F}(k, \varepsilon, \theta)}{d\varepsilon\, d\Omega} \right), \tag{1.10}$$

in terms of the cross-sections

$$\sigma_{S\gamma 1n}(k) + \sigma_{S\gamma np}, \sigma_{S\gamma 2n}(k), \ldots, \sigma_{S\gamma F}(k) \tag{1.11}$$

of the photoabsorption reactions (1.2)–(1.5), and in terms of the distribution of the neutrons produced in each of these reactions,

$$\frac{d^2 n_{S\gamma 1n}(k,\varepsilon,\theta)}{d\varepsilon\, d\Omega}, \quad \frac{d^2 n_{S\gamma 2n}(k,\varepsilon,\theta)}{d\varepsilon\, d\Omega}, \quad \ldots \frac{d^2 n_{S\gamma F}(k,\varepsilon,\theta)}{d\varepsilon\, d\Omega}. \tag{1.12}$$

In the expression (1.10), the sum runs over the number of emitted photoneutrons j, which is apparently restricted by the ordinary condition $k = E_\gamma > B_{Sjn}, B_{\rm SF}$, the threshold energies of the photonuclear reactions (1.2)–(1.5). The neutron emission angle θ is reckoned from the γ-flux direction that coincides with the direction of primary electron beam, as a matter of fact. Further, in Sec. 4, we shall mostly deal with the quantity (1.10) integrated over the total 4π solid angle,

$$Y_S(\varepsilon, E_e, J_e, R_S; t) = \frac{dn_S(\varepsilon, E_e, J_e, ; t)}{d\varepsilon} = \int d\Omega\, \Phi(\varepsilon, \theta, E_e(0), J_e, R_S; t), \tag{1.13}$$

that is the energy distribution of neutrons emitted in 4π solid angle per a unit of energy, per a unit of time.

The quantities (1.12) are normalized so that

$$\int d\varepsilon \int d\Omega \frac{d^2 n_{S\gamma 1n, S\gamma 2n, S\gamma F}(k,\varepsilon,\theta)}{d\varepsilon\, d\Omega} = 1. \tag{1.14}$$

They differ evidently from one another. The distributions (1.10), (1.13) depend on the sum of the products of each cross-section (1.11) and each respective distribution (1.12), unlike the total neutron yield

$$Y_S(E_e, J_e, R_S; t) = \int d\varepsilon \int d\Omega\, \Phi(\varepsilon, \theta, E_e(0), J_e, R_S; t), \tag{1.15}$$

determined just by the sum

$$\sigma_{S\gamma 1n}(k) + \sigma_{S\gamma np}(k) + 2\sigma_{S\gamma 2n}(k) + \ldots + \nu_{S\gamma nF}\sigma_{S\gamma F}(k), \tag{1.16}$$

immediately measured in experiments. The mean energy of neutrons is ordinarily defined through $Y_S(\varepsilon, E_e, J_e, R_S; t)$, $Y_S(E_e, J_e, R_S; t)$,

$$\bar{\varepsilon}_S(E_e, J_e, R_S) = \int \varepsilon\, d\varepsilon\, \frac{Y_S(\varepsilon, E_e, J_e, R_S; t)}{Y_S(E_e, J_e, R_S; t)}. \tag{1.17}$$

For the further discussion we also define the yield of neutrons with the energies ε greater than a given energy $\varepsilon_{\rm min}$,

$$\tilde{Y}_S(\varepsilon_{\rm min}, E_e, J_e, R_S; t) = \int\limits_{\varepsilon_{\rm min}}^{\infty} d\varepsilon\, Y_S(\varepsilon, E_e, J_e, R_S; t). \tag{1.18}$$

The photoabsorption cross-sections (1.11) were thoroughly measured in various experiments, and the reliable theoretical approaches were elaborated to describe the photoneutron distributions (1.12). It is instructive to split the total calculated quantity (1.10) into two parts,

$$\Phi_S(\varepsilon,\theta,E_e(0),J_e,R_S;t)=\Phi_{S\,k<\bar{k}}(\varepsilon,\theta,E_e(0),J_e,R_S;t)+ \\ +\Phi_{S\,k<\bar{k}}(\varepsilon,\theta,E_e(0),J_e,R_S;t). \quad (1.19)$$

The first one, $\Phi_{S\,k<\bar{k}}$, is the contribution to the total distribution Φ_S (1.10) from the integration over the absorbed photon energy $k \lesssim \bar{k}, \bar{k} \sim 20$ MeV. The second one, $\Phi_{S\,k>\bar{k}}$, is due to the integration over the large absorbed photon energy, $k \gtrsim \bar{k}$. These two contributions call for rather different treatments, which is explicated in the next sections.

2. THE GIANT-RESONANCE PHOTONEUTRONS

In this section, we treat the primary part, $\Phi_{S\,k<\bar{k}}$, of the general expression (1.10), that results from integration over the photon energy $k \lesssim \bar{k}$, $\bar{k} \sim 20$ MeV,

$$\Phi_{S\,k<\bar{k}}(\varepsilon,\theta,E_e(0),J_e,R_S;t)=J_e(t)\mathcal{N}_S^2\int\limits_0^{R_S}dx\int\limits_0^{\bar{k}}dk\frac{d\sigma_{Sb}(k,E_e(x,E))}{dk}\times \\ \times\left[1-\exp\left(\frac{x-R_S}{l_S(k)}\right)\right]l_S(k)\times \\ \times\left(\sum_{j=1,2,\ldots}j\sigma_{S\gamma jn}(k)\frac{d^2n_{S\gamma jn}(k,\varepsilon,\theta)}{d\varepsilon\,d\Omega}+\sigma_{S\gamma F}(k)\,\nu_{S\gamma nF}(k)\frac{d^2n_{S\gamma F}(k,\varepsilon,\theta)}{d\varepsilon\,d\Omega}\right). \quad (2.1)$$

The absorption of photons with energies $E_\gamma \lesssim 20$ MeV by heavy nuclei results in the giant resonance (GR) nuclear excitation. As the energy of an absorbed photon $E_\gamma \lesssim 20$ MeV $< B_{3n}$, i.e., the energy of the three neutrons emission threshold, the sum over j in $\Phi_{S\,k<\bar{k}}$ (2.1) contains only two terms with $j=1,2$.

In our calculations, we utilize the respective experimentally measured cross-sections (1.11) of the photoabsorption by uranium [10], by tantalum [11], and by lead [12] nuclei. For example, the cross-sections $\sigma_{\mathrm{U}\gamma 1n}(k)$, $\sigma_{\mathrm{U}\gamma 2n}(k)$, $\sigma_{\mathrm{U}\gamma F}(k)$ are displayed in Fig. 2, along with the γ flux (1.8) to induce nuclear excitations. As understood at once, the main contribution to neutron production comes from the area of GR, i.e., from the E_γ area, where these photoabsorption cross-sections

and the γ flux J_γ (1.8) overlap best of all. Now we are to acquire the photoneutron distributions (1.12) associated with each photoabsorption reaction. A lot of experiments on the energy and angular distribution of the GR photoneutrons proves that γ rays mostly produce the statistical neutrons, though there exists a small, yet discernible, fraction $\chi(k)$ of nonstatistical, «direct» neutrons as well (see, for instance, [13]), which shows up to be substantial at high photoneutrons energies, $\varepsilon \gtrsim 3$ MeV. As is generally received for the reactions with $E_\gamma \sim E_{\mathrm{GR}}$ [14], a nucleus remaining after direct neutron emission would never emit an additional neutron, yet the remainder of excitation energy is released as γ rays. Thus, in the GR energy area, no nonstatistical, fast neutrons are produced in the process (1.4).

The spectrum of statistical neutrons in the processes (1.2), (1.3), where a single neutron is emitted, can best be described by the Weisskopf statistical model [10, 14–17],

$$\frac{dn^{\mathrm{st}}_{\gamma 1n}(\varepsilon, k, Z, N)}{d\epsilon} = \varepsilon\, \exp\left[2\sqrt{\mathbf{a}(Z, N-1)(k - B_{1n} - \varepsilon)}\right] \times \\ \times\, \Theta(k - B_{1n} - \varepsilon)\, \Theta(\varepsilon - k + B_{2n}) \frac{1}{\mathcal{N}_{\gamma 1n}(k)}, \quad (2.2)$$

with the key suggestion that the second neutron would be always emitted whenever its emission were energetically possible [10, 14–17]. Here $\varepsilon = E_n - m_n$ is the neutron kinetic energy; $B_{1n}(Z, N)$, $B_{2n}(Z, N)$ are the thresholds of the reactions $(\gamma, 1n)$ and $(\gamma, 2n)$, respectively, and $\mathbf{a}(Z, N-1)$ stands for the nuclear level density parameter. In the calculations what follow, we utilize the $\mathbf{a}(Z, N)$ values that are given in [18]. The normalization factor $\mathcal{N}_{\gamma 1n}(k)$ is determined by the standard condition

$$\int_0^\infty d\varepsilon \frac{dn^{\mathrm{st}}_{\gamma 1n}(\varepsilon, k, Z, N)}{d\varepsilon} = 1. \quad (2.3)$$

In our treatment, we pursue the common suggestion that the cross-section of the inverse process $\sigma_{\mathrm{inv}}(\varepsilon)$, i.e., the cross-section of formation of a compound nucleus by neutron capture in the residual nucleus, is constant within the treated energy area [10, 14, 19, 20]. An optical model calculation could be made to allow for the energy dependence of $\sigma_{\mathrm{inv}}(\varepsilon)$, see, for instance, [19, 20], but in the present treatment this would not felt to be justified. As a matter of course, the contribution from statistical, evaporation neutrons, with the energy spectrum (2.2), to the distribution $\Phi_{S\,k<\bar{k}}$ (2.1) is angular isotropic,

$$\big(\sigma_{S\gamma n}(k) + \sigma_{S\gamma np}(k)\big) \frac{dn^{\mathrm{st}}_{\gamma 1n}\,(\varepsilon, k, \mathbf{a}(Z, N))}{d\varepsilon \cdot 4\pi} (1 - \chi(k)). \quad (2.4)$$

As is known, the statistical model fails to account completely for the observed photoneutrons energy and angular distribution [13]. The fraction $\chi(k)$ of the pre-

equilibrium, resonant-direct neutrons increases with the photon-energy E_γ growth, and one can infer from the findings of [17] that the linear relationship

$$\chi(E_\gamma) \approx 0.05\Theta(E_\gamma - B_{1n}(Z,N) - 2.5)(E_\gamma - B_{1n}(Z,N) - 2.5) \qquad (2.5)$$

holds to estimate the $\chi(E_\gamma)$ value within the GR photon-energy range. Yet, when χ (2.5) comes over 0.25, the value $\chi = 0.25$ will be set. All the energies are here implied to be given in MeV. So, there are no nonstatistical neutrons at $E_\gamma - B_{1n}(Z,N) < 2.5$ MeV, and at $E_\gamma \sim E_{\rm GR}$ the evaporation neutrons constitute about 0.75 of all the neutrons emitted. As was observed from [10, 15–17], the direct neutron spectra from heavy nuclei have peaks appreciably lower than the value of $\varepsilon \approx E_\gamma - B_{1n}(Z,N)$. As one infers from [10, 15–17], the resulting spectrum of nonstatistical, «direct» photoneutrons can safely be assumed to be constant between the values $(E_\gamma - B_{1n}(Z,N))$ and $\mathcal{D}(E_\gamma - B_{1n}(Z,N))$ of energy of a neutron, where $\mathcal{D}$ is a constant, $\mathcal{D} < 1$. The direct neutron intensity is assumed to be negligible at the smaller neutron energies. Consequently, we choose to approximate the direct neutron spectrum by the expression

$$\frac{dn^d_{S\gamma n}(\varepsilon, E_\gamma)}{d\varepsilon} = \frac{1}{1-\mathcal{D}} \int\limits_{\mathcal{D}}^{1} d\eta\, \delta(\varepsilon - \eta(E_\gamma - B_{1n}(Z,N))). \qquad (2.6)$$

Apparently, this $\sqcap$-shaped-function tends to $\delta(\varepsilon - E_\gamma + B_{1n}(Z,N))$ when $\mathcal{D} \to 1$, and the standard normalization holds

$$\int\limits_0^\infty d\varepsilon \frac{dn^d_{S\gamma n}(\varepsilon, E_\gamma)}{d\varepsilon} = 1. \qquad (2.7)$$

As was ascertained in [17], the value $\mathcal{D} = 0.4$ is preferable to describe the nonstatistical neutron production from deformed nuclei (alike U, W, Ta), whereas $\mathcal{D} = 0.7$ ought to be utilized in treating undeformed nuclei (alike Pb). Dependence of the computed neutron distribution on the $\mathcal{D}$ value will be treated further in Sec. 4.

As a dipole state is primarily excited by the γ-rays absorption, the angular distribution of pre-equilibrium, resonant-direct neutrons proves to be of the form $1 + C(\varepsilon)\sin^2(\theta)$ [13]. From the data presented in [17], one can derive the plausible estimations: $C(\varepsilon) = 0$ at $\varepsilon < e = 2.5$ MeV, and

$$C(\varepsilon) = \left\{ \begin{array}{cc} \dfrac{(\varepsilon - e)a}{(b-e)}, & \varepsilon < b \\ a, & \varepsilon > b \end{array} \right\},$$

with $a = 0.2$ MeV, $b = 5$ MeV for deformed nuclei, and $a = 0.8$ MeV, $b = 7.5$ MeV for undeformed ones. So, the properly normalized contribution to the

neutron distribution (2.1) from direct neutrons results in the form

$$\left(\sigma_{S\gamma n}(k)+\sigma_{S\gamma np}(k)\right)\frac{dn^{d}_{S\gamma n}(\varepsilon,k)}{d\varepsilon 4\pi}\chi(k)\frac{1+C(\varepsilon)\sin^2\theta}{1+2/3C(\varepsilon)}. \tag{2.8}$$

The expressions (2.4) and (2.8) together present the contribution to the quantity $\Phi_{k<\bar{k}}$ (2.1) from the single neutron emission after absorption of a photon with the energy $E_\gamma \lesssim 20$ MeV.

As is indicated above, the photoneutron production in the process (1.4) is described in the framework of the pure statistical approach. The energy distribution of the «first» of two neutrons emitted in the reaction (1.4) is written likewise Eq. (2.2):

$$\frac{dn^{\rm st}_{\gamma 2n}(\varepsilon,k,Z,N)}{d\varepsilon}=\varepsilon\,\exp\left[2\sqrt{\mathbf{a}(Z,N-1)(k-B_{1n}(Z,N)-\varepsilon)}\right]\times$$
$$\times\,\Theta(k-B_{2n}(Z,N)-\varepsilon)\frac{1}{\mathcal{N}_{\gamma 2n}(k)}, \tag{2.9}$$

normalized so that

$$\int\limits_0^\infty d\varepsilon\frac{dn^{\rm st}_{\gamma 2n}(\varepsilon,k,Z,N)}{d\varepsilon}=1. \tag{2.10}$$

With allowance for the general treatment developed in [14, 16], the energy distribution of the «second» neutron emitted in the reaction (1.4) is described as follows:

$$\frac{d\tilde{n}^{\rm st}_{\gamma 2n}(\varepsilon,k,Z,N)}{d\varepsilon}=\varepsilon\int\limits_0^\infty d\varepsilon'\,\varepsilon'\,\exp\left[2\sqrt{\mathbf{a}(Z,N-1)(k-B_{1n}(Z,N)-\varepsilon')}\right]\times$$
$$\times\exp\left[2\sqrt{\mathbf{a}(Z,N-2)(k-B_{2n}(Z,N)-\varepsilon-\varepsilon')}\right]\Theta(k-B_{1n}(Z,N)-\varepsilon')\times$$
$$\times\,\Theta(k-B_{2n}(Z,N)-\varepsilon-\varepsilon')\frac{1}{\mathcal{N}'_{\gamma 2n}(k)}, \tag{2.11}$$

and the normalization factor $\mathcal{N}'_{\gamma 2n}$ is determined accordingly to the condition

$$\int\limits_0^\infty d\varepsilon\frac{d\tilde{n}^{\rm st}_{\gamma 2n}(\varepsilon,k,Z,N)}{d\varepsilon}=1. \tag{2.12}$$

Surely, the angular distribution of evaporation neutrons is purely isotropic. So, at the absorbed photon energy $E_\gamma \lesssim 20$ MeV, the contribution to the distribution (2.1) from the process (1.4) is expressed through the sum of (2.9) and (2.11)

as follows:

$$\sigma_{S\gamma 2n}(k)\left(\frac{dn^{\rm st}_{\gamma 2n}(\varepsilon,k,Z,N)}{d\varepsilon}+\frac{d\tilde{n}^{\rm st}_{\gamma 2n}(\varepsilon,k,Z,N)}{d\varepsilon}\right)\frac{1}{4\pi}. \tag{2.13}$$

Given the absorbed photon energy $k=E_\gamma\lesssim 20$ MeV, the nuclear photofission (1.5) is accompanied by the angular isotropic emission of pure statistical neutrons, see [10, 21, 22], so that their contribution to the expression (2.1) is written as

$$\sigma_{S\gamma F}(k)\nu_{S\gamma F}(k)\,\mathbf{f}_{S\gamma F}(\varepsilon)\frac{1}{4\pi}, \tag{2.14}$$

with the emitted neutrons multiplicity

$$\nu_{{\rm U}\gamma F}(k)\approx 0.158k/{\rm MeV}+1.5 \tag{2.15}$$

for the ^{238}U photofission, which we shall utilize in what follows. The energy distribution of these neutrons is generally received (see [21, 22]) to be described by the function

$$\mathbf{f}_{{\rm U}\gamma F}(\varepsilon)=\frac{2\sqrt{\varepsilon}}{\sqrt{\pi T^3}}\,\exp\left(-\frac{\varepsilon}{T}\right),\quad T=\frac{4}{3}\ {\rm MeV}, \tag{2.16}$$

so as the mean energy of emitted neutrons shows up to be $\bar{\varepsilon}=2$ MeV.

Summarizing, the findings (2.4), (2.8), (2.13), (2.14) determine the part $\Phi_{k<\bar{k}}$ (2.1) of the total neutron distribution (1.10), (1.19).

3. THE NEUTRON PRODUCTION DUE TO HIGH-ENERGY BREMSSTRAHLUNG ABSORPTION

In this section, we calculate the part $\Phi_{k>\bar{k}}$ of the total neutron distribution (1.10) determined by integration over the absorbed photon energy $\bar{k}\lesssim k\lesssim k_{\max}$, with $\bar{k}\approx 20$ MeV, $k_{\max}\sim 100$ MeV. At energies above the giant resonance (GR), a γ quantum is primarily absorbed by the virtual quasi-deuteron, and there are also the surface absorption and the absorption due to the nucleon polarizability in nucleus [23].

Although the photo-absorption cross-sections (1.11) at these energies, $k=E_\gamma>20$ MeV, amount never more than ~ 20 mb, the quantity $\Phi_{k>\bar{k}}$ proves to be of value to describe the photoneutron spectrum, at high enough initial electron energy $E_e\sim 50{-}100$ MeV, because of a large number of photoneutrons accompanying the photoabsorption at these energies. At $E_\gamma\gtrsim 20$ MeV, the total photofission probability of the fissionable nucleus ^{238}U was found in [24, 25] to be equal to one, so that there occurs no sum over j in the distribution

$\Phi_{k>\bar{k}}$ (1.19), (1.10). The other way round, as was ascertained in [25–28], the photoneutrons production from hardly-fissionable nuclei Pb, Ta, W is completely described by the sum in (1.10) over the produced neutron multiplicity with $2 \leqslant j \lesssim 10$. In [24–29], the photoneutron production at these energies is described in terms of the total cross-sections of photon absorption at a given k, $\sigma_S(\mathrm{tot},\, k)$, and in terms of the mean multiplicity of direct (or fast) neutrons, $\bar{\nu}^d(k)$, and of statistical neutrons, $\bar{\nu}^{\mathrm{st}}(k)$, accompanying the photoabsorption. Then, the corresponding contribution to the whole distribution (1.10) is written in the form

$$\Phi_{Sk>\bar{k}}(\varepsilon,\theta,E_e(0),J_e,R_S;t) = J_e(t)\mathcal{N}_S^2 \int\limits_0^{R_S} dx \times$$

$$\times \int\limits_{\bar{k}}^{k_{\max}} dk \frac{d\sigma_{Sb}(k,E_e(x))}{dk} \left[1-\exp\left(\frac{x-R_S}{l_S(k)}\right)\right] l_S(k)\sigma_S(\mathrm{tot},k)\times$$

$$\times \left(\bar{\nu}_S^{\mathrm{st}}(k)\frac{d^2n_S^{\mathrm{st}}(k,\varepsilon,\theta)}{d\varepsilon\, d\Omega} + \bar{\nu}_S^d(k)\frac{d^2n_S^d(k,\varepsilon,\theta)}{d\varepsilon\, d\Omega}\right), \quad (3.1)$$

where the index $S = \mathrm{U},\ \mathrm{Ta},\ \mathrm{Pb}$ designates the sort of material of the irradiated sample. Values of the cross-sections $\sigma_S(\mathrm{tot},k)$ and of the mean multiplicity $\bar{\nu}_S^{\mathrm{st}}(k), \bar{\nu}_S^d(k)$, we utilize in what follows, are deduced from the findings of [24–29]. The total mean number of photoneutrons $\bar{\nu}_S(k) = \bar{\nu}_S^{\mathrm{st}}(k) + \bar{\nu}_S^d(k)$ rangers from 2 up to ~ 10, with the absorbed photon energy varying within the limits $20 \lesssim E_\gamma \lesssim 100$ MeV. The multiplicity $\bar{\nu}_S^d(k)$ constitutes about 10–20% to $\bar{\nu}_S^{\mathrm{st}}(k)$.

Firstly, we compute the distribution (3.1) for nonfissionable nuclei. For each photon absorbed by Ta, Pb nuclei, there remains a residual excited nucleus after fast particles have escaped from an initial nucleus. In the calculations what follow, a type of the residual nucleus, as well as its excitation energy, are obtained amenably to [25, 27–29] from the absorbed photon energy, and energies of the particles that have escaped nucleus. Let $\bar{E}^*$ be the average excitation energy of the residual compound nucleus, i.e., the excited nucleus left after all fast processes has taken place. For the treated Ta, Pb nuclei, the residual compound nuclei decay by neutron evaporation, and, pursuant to [27, 28], the expression holds:

$$\bar{E}_S^*(k) = (\bar{B}_S' + 2\bar{\vartheta}_S(k))\bar{\nu}_S^{\mathrm{st}}(k) + \bar{B}_S/2, \quad (3.2)$$

where the quantity $2\bar{\vartheta}_S(k) = \bar{\varepsilon}(k)$ corresponds to the mean kinetic energy of evaporated neutrons, according to the standard statistical approach. In Eq. (3.2), $\bar{B}_S$ is the mean binding energy of the final residual nucleus in an evaporation

chain, whereas $\bar{B}'_S$ stands for the average binding energy of nuclei in the chain. On the other hand, the average excitation energy $\bar{E}^*_S(k)$ (3.2) is generally received (see, for instance, [14, 16, 27, 28]) to be related to the parameter $\bar{\vartheta}_S(k)$ through the nuclear level density parameter $\mathbf{a}(Z,N)$,

$$\bar{E}^*_S(k) = \mathbf{a}(Z,N)\,\bar{\vartheta}^2_S(k). \tag{3.3}$$

Combining Eqs. (3.2) and (3.3), we obtain

$$\bar{\vartheta}_S(k) = \frac{\bar{\nu}^{\rm st}_S(k) + \sqrt{\bar{\nu}^{\rm st}_S(k) + \mathbf{a}(Z,N)\bigl(\bar{\nu}^{\rm st}_S(k) + \bar{B}'_S + 0.5\bar{B}_S\bigr)}}{\mathbf{a}(Z,N)}. \tag{3.4}$$

The quantities $\bar{B}'_S$, $\bar{B}_S$ are evaluated using the data presented in [30], and the $\mathbf{a}(Z,N)$ values are taken from [18]. The statistical evaporation neutron distribution involved in $\Phi_{Sk>\bar{k}}$ (3.1) is commonly chosen in the form

$$\frac{d^2n^{\rm st}_S(k,\varepsilon,\theta)}{d\varepsilon\,d\Omega} = \frac{1}{4\pi}\frac{\sqrt{\varepsilon}}{\sqrt{\pi T^3(k)}}\exp\left(-\frac{\varepsilon}{T(k)}\right), \tag{3.5}$$

with the temperature parameter T determined by the condition

$$\bar{\varepsilon}_S(k) = 2\bar{\vartheta}_S(k) = \int \varepsilon\,d\varepsilon\,4\pi\frac{d^2n^{\rm st}_S(k,\varepsilon,\theta)}{d\varepsilon\,d\Omega} = \frac{3T(k)}{2}. \tag{3.6}$$

Apparently, the distribution (3.5) is properly normalized,

$$\int d\varepsilon \int d\Omega\,\frac{d^2n^{\rm st}_S(k,\varepsilon,\theta)}{d\varepsilon\,d\Omega} = 1. \tag{3.7}$$

The direct photoneutron distribution in expression (3.1) is chosen, alike above in Sec. 2, see Eqs. (2.6), (2.8), in the form

$$\frac{d^2n^{d}_S(k,\varepsilon,\theta)}{d\varepsilon\,d\Omega} = \frac{dn^{d}_S(k,\varepsilon)}{d\varepsilon\,4\pi}\frac{1 + C(\varepsilon)\sin^2\theta}{1 + (2/3)C(\varepsilon)}. \tag{3.8}$$

In treating the neutron production $\Phi_{{\rm U}k>\bar{k}}$ (3.1) from uranium due to γ-rays absorption with $k = E_\gamma > 20$ MeV, we put to use the total photoabsorption cross-sections $\sigma_{\rm U}({\rm tot},k)$ in (3.1) that were measured in [24, 26]. The statistical neutrons distribution in (3.1) is written, just alike (2.14), in the form

$$\frac{d^2n^{\rm st}_{\rm U}(k,\varepsilon,\theta)}{d\varepsilon\,d\Omega} = \frac{1}{4\pi}\,\mathbf{f}_{{\rm U}\gamma F}(\varepsilon), \tag{3.9}$$

with the function $\mathbf{f}_{{\rm U}\gamma F}(\varepsilon)$ given by Eq. (2.16). The distribution of direct (fast) neutrons accompanying uranium photofission is given again in the form (3.8) with $S = {\rm U}$.

Thus, for all the considered nuclei, both nonfissionable, Ta, Pb, and fissionable, U, we have obtained the part $\Phi_{Sk>\bar{k}}$ (3.1) of the total neutron distribution (1.10).

At last, adding the calculated quantities $\Phi_{Sk<\bar{k}}$ and $\Phi_{Sk>\bar{k}}$, we obtain according to Eq. (1.19) the required distributions (1.10), (1.15), (1.13) of neutrons produced from a given sample, irradiated by an electron beam with a given energy E_e and current density J_e.

Recapitulating the consideration carried out, we realize that the treatment of neutron distribution shows up to be substantially model-dependent. Though the physical approaches that we pursue are believed to be well justified, the calculations carried out involve inescapable ambiguities, so that, strictly speaking, the results we have obtained are to be considered as being semiquantitative, as a matter of fact. Notwithstanding, as we shall become convinced in the next section, our treatment is suitable to describe the observed neutron flux, all the more that the experimental data available for now are understood to have got the discernible uncertainties.

4. FINDINGS DISCUSSION

In this section, we present the outcome of our calculations and successively compare our findings with the experimental measurements of characteristics of the neutron flux generated from U, Ta, and Pb samples. The results are displayed in Figs. 3–7 and in Tables 1 and 2.

A real electron beam cannot be just monoenergetic, and, strictly speaking, the electron energy distribution in a beam, $\rho_e(E)$, ought to have been taken into consideration, alike what was done in [3]. Yet so far as the width of the distribution $\rho_e(E)$ in all the actual cases is much smaller than the mean electron energy $\bar{E} = E_e$, it is natural that all the calculations are merely carried out with the mean electron energy. Certainly, the findings can be directly integrated over a given energy distribution, when required.

The results further discussed are expressed through the average electron current $\bar{J}_e$ of a considered e-linac. Consequently, we obtain the average neutron flux Y. As the neutron yield is plainly proportional to the beam current, the neutron flux within a pulse, $Y^{\rm pulse}$, is merely obtained with replacing the average current $\bar{J}_e$ by the current in a pulse, $J_e^{\rm pulse}$, which results in $Y^{\rm pulse} = Y/\Delta t \nu_t$, where Δt is the pulse length and ν_t is the pulse repetition rate. For instance, the further discussed GELINA neutron source operates with $\Delta t = 1$ ns, $\nu_t = 800$ Hz, $J_e^{\rm pulse} = 120$ A, so that $\bar{J}_e = 96$ μA. Then, within a 1 ns pulse, the neutron production of $4.3 \cdot 10^{10}$ neutrons is achieved, when $Y = 3.4 \cdot 10^{13}$ n $\cdot$ s^{-1}.

Surely, all the energy and the charge of the incident electron beam are to be deposited within the irradiated sample. Consequently, an actual experimental

setup is arranged so that the transverse size of electron beam would be smaller than (or at least equal to) the irradiated sample transverse size. The center of the beam spot on the sample surface is natural to coincide with the center of the sample transverse area. Thus, the active neutron-creation volume turns out actually to be a cylinder with a transverse area equal to the beam spot and with a longitudinal size equal to the thickness R_S of irradiated sample (see Fig. 1), no matter how complicated a real sample construction would be. Let us recall that saturation of the neutron yield sets in above the cylinder length $R_S \approx 4{-}6$ cm, see [3]. Of course, we shall compare the results of measurements and evaluations carried out at the equal R_S values.

The total neutron flux and the spectrum of neutrons emitted from an irradiated target are influenced by inelastic collisions in radiator material itself. Thus, the neutron energy distribution we have been treating does not coincide with the distribution of neutrons that escape radiator. The calculated spectrum can stand for the spectrum of neutrons emitted from radiator only if it is suggested that neutrons are not attenuated in passing through sample material after being produced. Surely, the neutrons escape is desired to be as close to the production as possible. As is realized, the neutrons escape from the cylindrical geometry radiator is superior to the escape from other radiator constructions. Let the longitudinal size of a radiator be ~ 5 cm, as discussed above, and its transverse area be about a few cm^2, which typifies dimensions of radiators of the really acting neutron sources. Then, the mean distance $\bar{L}$ that a produced photoneutron covers until leaving the radiator proves to be ~ 2 cm. For the materials we deal with, Ta, W, U, Pb, the cross-sections $\sigma_{\rm INL}(\varepsilon)$ of neutron inelastic collisions constitute never more than $\sim 1{-}2$ b, at the neutron energies really presented in the photoneutron spectrum (see, for instance, [31]). The mean free path for the inelastic scattering is estimated as

$$L_{\rm INL} \approx (\mathcal{N}_S \cdot \sigma_{\rm INL})^{-1} \approx 10{-}12 \text{ cm}, \tag{4.1}$$

which shows up to be appreciably greater than $\bar{L}$. That is why our findings suite for describing the emitted neutrons spectra. Clearly, above certain dimensions of a radiator, the extra material serves as an absorber or moderator. Then, for each one experimental set-up, the optimum dimensions of irradiated cylindrical sample are to be evaluated with allowance for the neutron production and escape probability.

In performing the computations further discussed, we utilized the required values of physical quantities provided in the references cited in the previous Secs. 1–3.

The dotted curve in Fig. 3 stands for the computed energy distribution (1.13) of the neutrons produced from a thick ^{238}U sample by an electron beam with the initial energy $E_e = 105$ MeV and current $\bar{J}_e = 96$ μA, which are the standard

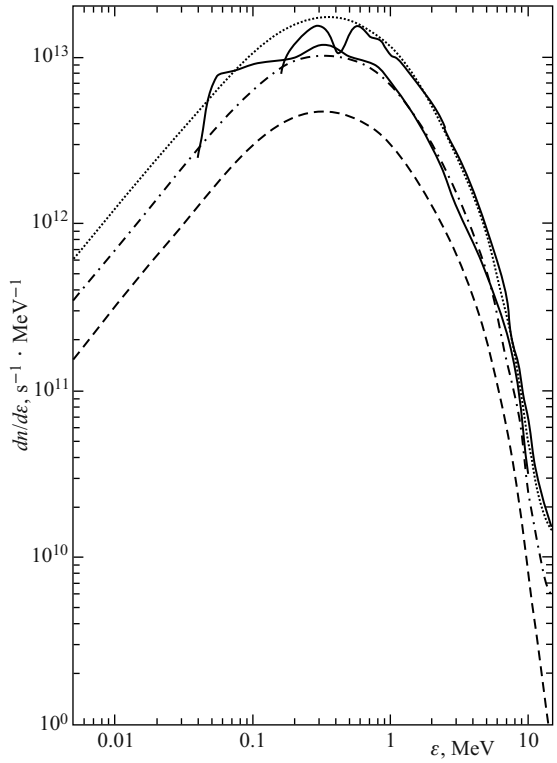

Fig. 3. The spectra of neutrons generated by electron beams of different energies E_e and currents $\bar{J}_e$ from a thick U sample, $R_S \gtrsim 5$ cm. The thick and thin solid curves stand for the neutron spectra at $E_e = 100$ MeV, $\bar{J}_e = 100$ μA, and at $E_e = 55$ MeV, $\bar{J}_e = 100$ μA, respectively, which are derived from the data presented in [32–35] and in [38], as discussed in the text. The dotted, dash-dotted, and dashed curves represent our calculations at $\bar{J}_e = 100$ μA and $E_e = 100$ MeV, $E_e = 55$ MeV, $E_e = 30$ MeV, respectively

performances of the GELINA facilities, as designated in Table 1 of [32]. Let us mention that the respective computed total neutron yield Y (1.15) is in agreement with one asserted in [32–35], as is seen in Table 1. Now we aim to correlate the calculated neutron spectrum (the dotted curve in Fig. 3) with the findings of measurements presented in [32–35], which calls for the particular consideration what follows. The measured neutron spectrum is presented in Fig. 4, *b* in [33] (as well as in Fig. 5 in [34] and in Fig. 2 in [35]) in terms of neutron flux per a unit of lethargy, at the $\theta = 90^\circ$ angle with respect to electron beam direction, and at the distance $L_{\rm path} = 200$ m from the neutron hot spot. Let us denote

Table 1. **The total yields Y and mean energies $\bar{\varepsilon}$ of the neutrons generated by an electron beam with the initial energy E_e (MeV) and average current $\bar{J}_e$ (10 μA) from irradiated U, Ta, Pb samples, as designated in the first row, with the thickness R_S (cm). $\bar{\varepsilon}_{S\,\mathrm{comp}}$ (MeV) and $Y_{S\,\mathrm{comp}}$ (10^{11} s^{-1}) are the computed quantities, whereas $\bar{\varepsilon}_{S\,\mathrm{exp}}$ (MeV) and $Y_{S\,\mathrm{exp}}$ (10^{11} s^{-1}) are obtained from the experimental data, when available**

Sample	^{238}U*	^{238}U**	^{238}U	^{181}Ta***	^{181}Ta****	^{181}Ta	$^{\mathrm{nat}}$Pb*****	$^{\mathrm{nat}}$Pb******
R_S	$\gtrsim 5$	$\gtrsim 5$	5	≈ 7	3.175	5	1.68	1.12
E_e	105	55	30	65	140	30	45	30
$\bar{J}_e$	10	10	10	0.09	1	1	100	100
$\bar{\varepsilon}_{\mathrm{comp}}$	1.66	1.63	1.56	1.65	1.76	1.46	1.59	1.47
$\bar{\varepsilon}_{\mathrm{«exp»}}$	1.61	1.69		1.7	~ 1.8		1.7	1.40
Y_{comp}	310	180	78.5	1	17.2	3.5	560	195
$Y_{\mathrm{«exp»}}$	340	189		1	18.2		540	190

*The «exp» data from [32–35].
**The «exp» data from [38].
***The «exp» data from [40].
****The «exp» data from [39].
*****The «exp» data from [42, 43].
******The «exp» data from [44, 45].

this measured spectrum by

$$\Phi_{\mathrm{GELINA}}(\varepsilon) = \varepsilon \frac{dn_{\mathrm{GELINA}}(\varepsilon, L_{\mathrm{path}}, \theta, R_{\mathrm{U}}, E_e, \bar{J}_e)}{d\varepsilon}\ [\mathrm{s}^{-1}]. \tag{4.2}$$

Inquiring into construction of the GELINA rotary target, one realizes that there is an amount of heavy material between the detector and the neutron creation volume. That material amount varies with the angle of detector location, increasing from the conceivable zero value at $\theta = 180^\circ$ angle, i.e., in backward direction, up to its maximum value at the $\theta = 0^\circ$ angle, i.e., in forward direction. This heavy material of the target scatters neutrons away from the track towards detector. Upon close inquiring into the findings presented in Fig. 3 in [32] and in Fig. 5 in [34], we understand that there appears about three-fold decrease of the primary neutron flux at the $\theta = 90^\circ$ angle. So, to allow for this attenuation, the aforesaid spectrum (4.2) in [32, 33] mast be multiplied by the factor $C_t \approx 3$.

Two ^{10}B filters of 0.46 and 0.645 g/cm^2, and one $^{\mathrm{nat}}$U disc of 36.137 g/cm^2 were placed at the 100 m station, upon neutrons passing the precollimation. The modification of the primary neutron flux because of these filters can be estimated

with multiplying it by the factor

$$C_{\mathrm{BU}}(\varepsilon) = \exp\big[(\sigma_{\mathrm{B}n\,\mathrm{tot}}(\varepsilon)\cdot 1.105/10 + \\ + \sigma_{\mathrm{U}n\,\mathrm{tot}}(\varepsilon)\cdot 36.137/238)6.0022\cdot 10^{23}\big], \quad (4.3)$$

where the total cross-sections $\sigma_{\mathrm{B}n\,\mathrm{tot}}(\varepsilon)$, $\sigma_{\mathrm{U}n\,\mathrm{tot}}(\varepsilon)$ of neutron interaction with uranium and boron are taken from [36, 37].

The 4π neutron flux we are in need of is obtained from the flux described in Fig. 4, *b* in [33] with multiplying that by the area of sphere

$$S_L = 4\pi L_{\mathrm{path}}^2, \quad (4.4)$$

with $L_{\mathrm{path}} = 200$ m.

A neutron flux per a unit of energy, $dn/d\varepsilon$ ($\mathrm{s}^{-1}\cdot\mathrm{MeV}^{-1}$), is just obtained with dividing a flux per a unit of lethargy, $\varepsilon\, dn/d\varepsilon$ (s^{-1}), at neutron energy ε.

As is observed, the measurements discussed in [33, 35] were performed with $\bar{J}_e = 70$ μA instead of $\bar{J}_e = 100$ μA, so that the data presented in Fig. 4, *b* in [33] should still be multiplied by the factor $C_J = 100/70$, when correlated with our results presented by the dotted curve in Fig. 3.

Eventually, the measured distribution (4.2) corresponds to the neutron 4π flux per a unit of energy

$$Y_{\mathrm{U\ exp}}(\varepsilon, E_e, \bar{J}_e, R_{\mathrm{U}}) = \frac{dn_{\mathrm{U\ exp}}(\varepsilon, E_e, \bar{J}_e, R_{\mathrm{U}})}{d\varepsilon} = \\ = \varepsilon\frac{dn_{\mathrm{GELINA}}(\varepsilon, L_{\mathrm{path}} = 200\ \mathrm{m}, \theta = 90^\circ, R_{\mathrm{U}}, E_e = 105\ \mathrm{MeV}, \bar{J}_e = 70\ \mu\mathrm{A})}{d\varepsilon}\times \\ \times\,[\varepsilon^{-1}\cdot S_L\cdot C_J\cdot C_{\mathrm{BU}}^{-1}(\varepsilon)\cdot C_t], \quad (4.5)$$

generated from a thick uranium sample by the electron beam with $E_e = 105$ MeV, $\bar{J}_e = 100$ μA. Just this spectrum (4.5), restored from the experimental observation (4.2), is displayed in Fig. 3 by the thick solid curve that should be correlated with the dotted curve standing for the respective calculated neutron spectrum. As is seen, the experimental and calculated spectra can be considered to be compatible satisfactorily with each other, especially keeping in mind the ambiguities associated with the transformation (4.5) from the immediate experimental observation (4.2) to the primary neutron spectrum.

In Fig. 3, the dash-dotted curve stands for the computed energy distribution (1.13) of the neutrons generated from a thick uranium sample by an electron beam with $E_e = 55$ MeV, $\bar{J}_e = 100$ μA. The spectrum of neutrons produced from a thick uranium sample by an electron beam with $E_e = 55$ MeV, $\bar{J}_e = 240$ μA was measured in [38]. In these measurements, the 2 cm thick B_4C filter and the 3.6 cm thick W filter were interposed in the neutron flux, upon it passing

the collimator. Therefore, to be compared with our calculation, the spectrum measured in [38] should be multiplied by the factor

$$\exp\left((\rho_{\mathrm{W}}\sigma_{\mathrm{W}n\,\mathrm{tot}}(\varepsilon)3.6/184+(4\rho_{\mathrm{B}}\sigma_{\mathrm{B}n\,\mathrm{tot}}(\varepsilon)+\right.$$
$$\left.+\rho_{\mathrm{C}}\sigma_{\mathrm{C}n\,\mathrm{tot}}(\varepsilon))2/52)6.022\cdot 10^{23}\right), \quad (4.6)$$

where ρ_{W}, ρ_{B}, ρ_{C} are the tungsten, boron, and carbon densities, and the total cross-sections of neutron interaction with W, B, C are taken from [36, 37]. In addition, as the spectrum in [38] was measured with $\bar{J}_e = 240$ μA instead of $\bar{J}_e = 100$ μA, it must be multiplied by the factor 100/240, when compared with our calculation. Then, after these transformations, the measured in [38] neutron spectrum gets displayed by the thin solid curve in Fig. 3. Comparing this curve with the dash-dotted curve, we can judge to what extent our treatment is of success in describing this experimentally observed spectrum. As is seen, agreement between the calculated and measured spectra shows up to be rather satisfactory at $\varepsilon \gtrsim 0.2$ MeV. Of course, one must realize that the discussed experimental data themselves cannot be thought to be quite unambiguous and unsophisticated.

For the sake of generality, we also present in Fig. 3 the calculated spectrum of neutrons generated from a thick uranium sample by an electron beam with the smaller energy $E_e = 30$ MeV.

It is quite desirable and instructive to correlate the results of calculations with the experimental measurements. Therefore, though our treatment is, strictly speaking, valid for $E_e \lesssim 100$ MeV, we dare to consider the neutron production from tantalum by the electron beam with $E_e = 140$ MeV, as the reliable measurement of the neutron spectrum from Ta sample exists for now only at this electron energy [39]. Derived from the data presented in [39], the solid curve in Fig. 4 presents the energy distribution of the neutron flux (1.13) generated from the 3.175 cm thick tantalum sample by the electron beam with $E_e = 140$ MeV, $\bar{J}_e = 10$ μA. The dotted curve in Fig. 4 stands for our respective calculation. As is seen, the agreement between these curves can be thought to be rather satisfactory.

The three blobs in Fig. 4 ought to have conformed to the dash-dotted curve, so far this curve stands for the neutron spectrum (1.13) calculated with the sample and beam parameters, $R_{\mathrm{Ta}} \gtrsim 5$ cm, $E_e = 65$ MeV, $\bar{J}_e = 10$ μA, the measurements in [40] were performed with. Yet, there is no wonder that they do not, as the multiple-foil activation method, applied in [40], is hardly believed to provide more than a crude estimation of the neutron spectrum.

The dashed curve in Fig. 4 is obtained with the same values $R_{\mathrm{Ta}} \gtrsim 5$ cm, $\bar{J}_e = 10$ μA, yet with the smaller electron beam energy $E_e = 30$ MeV.

Let us recall that all the neutron distributions involve the discernible contribution from the nonstatistical neutrons, governed by the value of the parameter $\mathcal{D}$

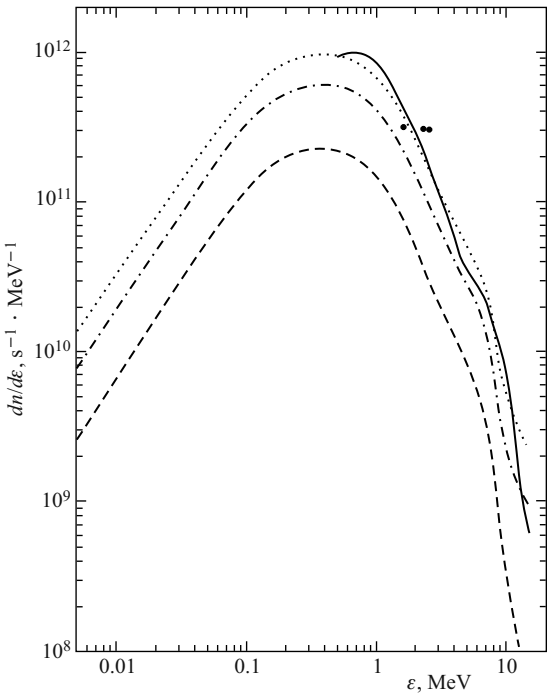

Fig. 4. The spectra of neutrons generated by electron beams of different energies E_e and currents $\bar{J}_e$ from tantalum samples of various thickness $R_{\rm Ta}$. The solid curve describes the neutron spectrum at $E_e = 140$ MeV, $\bar{J}_e = 10$ μA, $R_{\rm Pb} = 3.175$ cm, which is derived from the measurements of [39], as discussed in the text. The blobs correspond to the data obtained in [40]. Our calculations according to Eq. (1.13) are presented by the dotted curve for $E_e = 140$ MeV, $\bar{J}_e = 10$ μA, $R_{\rm Ta} = 3.175$ cm, by the dash-dotted curve for $E_e = 65$ MeV, $\bar{J}_e = 10$ μA, $R_{\rm Ta} = 5$ cm, and by the dashed curve for $E_e = 30$ MeV, $\bar{J}_e = 10$ μA, $R_{\rm Ta} = 5$ cm. This computations are carried out with the parameter $\mathcal{D} = 0.4$ in Eq. (2.6) rendering the energy distribution of nonstatistical neutrons

in Eq. (2.6). We dealt heretofore with deformed nuclei of uranium and tantalum, and the value $\mathcal{D} = 0.4$ was utilized. As understood from Eq. (2.6), increase of $\mathcal{D}$ value results in augmentation of the direct neutron contribution to neutron flux. It stands to reason to examine the influence of $\mathcal{D}$ value on neutron spectrum. For that matter, we present in Fig. 5 the same neutron spectra as in Fig. 4, yet evaluated with $\mathcal{D} = 0.7$, in order to emphasize the direct neutrons contribution. As is seen, the evaluated spectra undergo thereby noteworthy modifications, within the neutron energy area $3 \lesssim \varepsilon \lesssim 7$ MeV. It is to point out that the behavior of the spectrum of neutrons generated from Ta sample at $E_e = 30$ MeV pre-

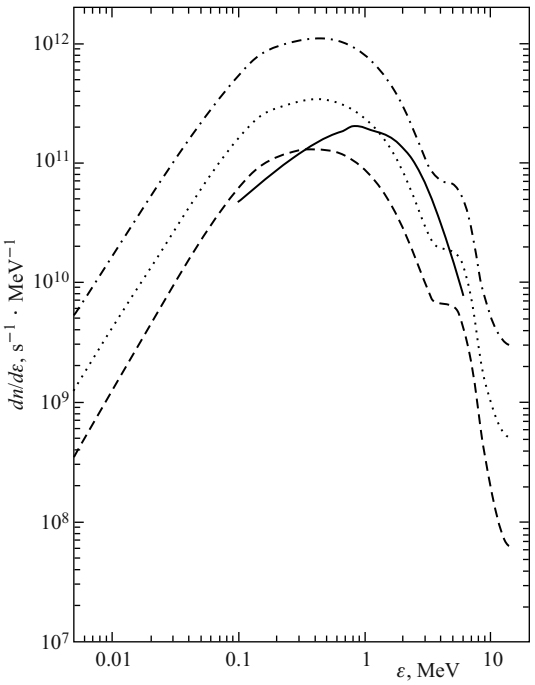

Fig. 5. The same as in Fig. 4, yet for $\mathcal{D} = 0.7$

sented in Fig. 5 is akin to the behavior of the respective spectrum ascertained in [41].

It is also to the point to discuss briefly the angular distribution of the neutron flux intensity, which is understood to be due to the nonstatistical, direct neutrons contributions (2.6), (2.8), (3.8). To make the θ-dependence conspicuous, let us draw into consideration the flux of neutrons with energies greater than a given value ε_m, at a given angle θ,

$$\frac{dn_S(\theta, E_e, \bar{J}_e, R_S; t)}{d\Omega} = \int\limits_{\varepsilon_m}^{\infty} d\varepsilon\, \Phi(\varepsilon, \theta, E_e, \bar{J}_e, R_S; t), \tag{4.7}$$

derived from Eq. (1.10). In the case of the considered tantalum sample, at $\varepsilon_m = 3$ MeV, the difference between the values of this quantity (4.7) at $\theta = \pi/2$ and $\theta = 0$ constitutes about 15%, which typifies the θ dependence of a photoneutron flux produced from heavy nuclei.

In Fig. 6, the thick solid curve stands for the energy distribution (1.13) of neutrons generated from the lead sample 1.68 cm thick by the electron beam with

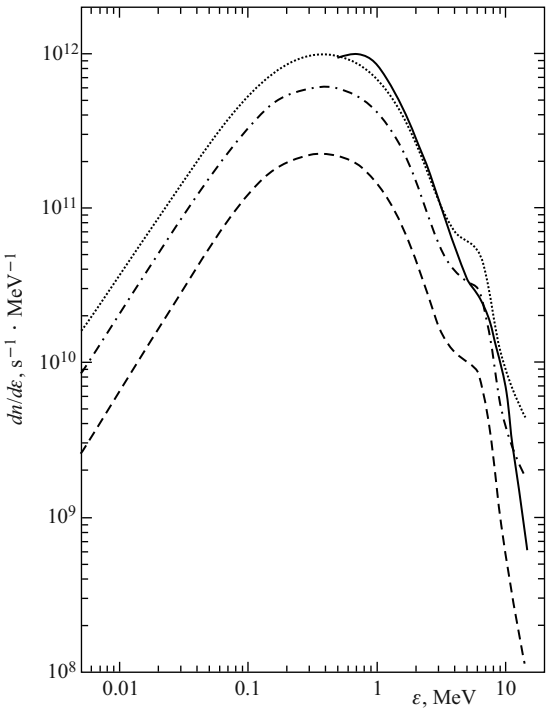

Fig. 6. The spectra of neutrons generated by electron beams with different energies E_e and currents $\bar{J}_e$ from lead samples of various thickness $R_{\rm Pb}$. The solid curve stands for the spectrum corresponding to $E_e = 45$ MeV, $\bar{J}_e = 1$ mA, $R_{\rm Pb} = 1.68$ cm, asserted in [42, 43]; the dotted curve presents our calculation with the same E_e, $\bar{J}_e$, $R_{\rm Pb}$. The dash-dotted and dashed curves display the computed neutron spectra at $E_e = 100$ MeV, $\bar{J}_e = 1$ mA, $R_{\rm Pb} = 6$ cm and at $E_e = 30$ MeV, $\bar{J}_e = 1$ mA, $R_{\rm Pb} = 1.12$ cm, respectively

$E_e = 45$ MeV, $\bar{J}_e = 1$ mA, as was procured in [42, 43]. It is to emphasize that, in this case, we deal not with pure experimental measurements, for lack of those by now, yet with some numerical simulation. The outcome of our respective computation is displayed by the dotted curve, that differs apparently from the aforesaid solid curve. So, our findings can scarcely be conformed to the results of numerical simulations in [42, 43], concerning the neutron spectrum description.

The dashed curve in Fig. 6 displays the evaluated spectrum (1.13) of neutrons generated from the 1.12 cm thick liquid lead sample by the electron beam with $E_e = 30$ MeV, $\bar{J}_e = 1$ mA, which are announced to be the standard performances of the neutron source ELBE, see [44–46]. Lacking by now in the respective ex-

perimental data, it is natural to correlate our findings with the results of respective numerical simulations carried out in [44,45]. For that purpose, we have processed our outcome, represented by the dashed curve in Fig. 6, and figure it in the form used in [44,45]. Consequently, Fig. 7 shows the energy distribution of the neutron flux at the measuring position $L_{\rm path} = 3.9$ m from the 1.12 cm thick liquid lead radiator for $E_e = 30$ MeV, $\bar{J}_e = 1$ mA. The width of the energy bins in Fig. 7 is equally distributed on the logarithmic scale. As is seen, either spectra displayed in Fig. 7 turn out to be in rather satisfactory agreement, except for the neutron energy $\varepsilon \gtrsim 2$ MeV, where the results of our calculation appreciably exceed the results of the numerical simulations in [44, 45]. That is thought to be due to the direct neutron contribution (2.6) for undeformed lead nucleus.

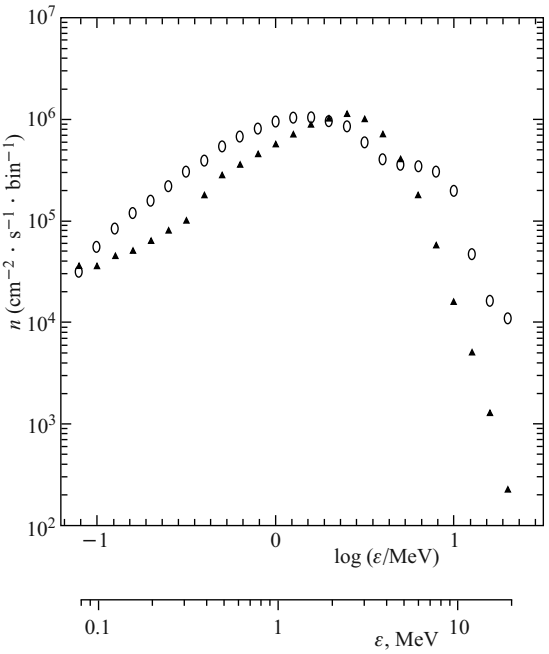

Fig. 7. The neutron flux energy distribution at the measuring position $L = 3.9$ m from the 1.12 cm thick liquid lead radiator (for each neutron energy bin) with $E_e = 30$ MeV and $\bar{J}_e = 1$ mA. The empty circles present the results of [44, 45], and the triangles stand for our results

The discussions in general terms, concerning the feasible spectrum of neutrons produced at various sources, can be found in some other publications, see, for instance, [1, 46–48]. The findings of these investigations corroborate in essence our calculations.

As is known, the operation of a number of modern setups (see, i.e., [2]) is associated with the nuclear reactions

$$n + {}^{238}\mathrm{U} \longrightarrow \gamma + {}^{239}\mathrm{U}^{*}, \tag{4.8}$$

$$n + {}^{238}\mathrm{U} \longrightarrow \gamma + n + {}^{238}\mathrm{U}^{*}, \tag{4.9}$$

$$n + {}^{238}\mathrm{U} \longrightarrow 2n + {}^{237}\mathrm{U}^{*}, \tag{4.10}$$

$$n + {}^{238}\mathrm{U} \longrightarrow 3n + {}^{239}\mathrm{U}^{*}, \tag{4.11}$$

$$\ldots\ldots\ldots\ldots\ldots\ldots\ldots\ldots$$

$$n + {}^{238}\mathrm{U} \longrightarrow \text{fission fragments} + \nu_{nF}\ \text{fission neutrons}, \tag{4.12}$$

induced by the neutron flux in a uranium bulk. The cross-sections of these reactions essentially depend on the incident neutron energy. The first reaction (4.8) runs successfully provided $\varepsilon \lesssim 1$ MeV [49]. The reaction (4.9) has actually got the threshold about 0.1–0.2 MeV [31]. The effective threshold of the uranium fission by neutrons constitutes ≈ 1 MeV [49, 50]. The reaction (4.10) with two neutrons in final state is really possible when $\varepsilon \gtrsim 4{-}5$ MeV [51]. Surely, the greater number of neutrons are produced, the greater the threshold of the respective reaction is. In treating neutron interactions in uranium medium, we are to realize what a share of the total neutron flux determines actually each of the processes (4.8)–(4.12). The quantity $\tilde{Y}(\varepsilon_{\min})$ (1.18) serves to meet this case. Table 2 represents the calculated neutron flux with energies ε greater than a certain energy $\varepsilon_{\min}$. As is seen, even at a large enough $\varepsilon_{\min}$, the neutron flux $\tilde{Y}(\varepsilon_{\min})$ is considerable. For instance, in the case considered in Table 2, one-half of neutrons amount is enable to induce uranium fission.

Table 2. **The yields $\tilde{Y}(\varepsilon_{\min})$ (1.18) of neutrons with energies greater than $\varepsilon_{\min}$ (MeV), generated by the electron beam with the initial energy $E_e = 55$ MeV and average current $\bar{J}_e = 100$ μA from irradiated ^{238}U thick sample**

$\varepsilon_{\min}$														
Energy	~ 0	0.1	0.2	0.5	1.0	1.5	2	2.5	3	4	5	6	7	10
$\tilde{Y}(\varepsilon_{\min})$	180	176	168	138	96	68	50	37	28	16	9.1	5.3	3.3	1.1

For each considered electron beam and irradiated sample, the respective average neutron energy $\bar{\varepsilon}_{S=\mathrm{U,Ta,Pb}}(E_e, \bar{J}_e, R_S)$ (1.17), and the total neutron yield $Y_{S=\mathrm{U,Ta,Pb}}(E_e, \bar{J}_e, R_S; t)$ (1.15) are presented in Table 1. The index «exp» is prescribed both to the actual experimental data and to the values obtained through some numerical simulations, so far as the real measurements are absent for now. It is to mention that increase of the mean neutron energy $\bar{\varepsilon}$ is rather indiscernible with E_e growth. As is seen from Table 1, in all the cases considered, the calculated and experimental values of the spectrum-integrated quantities Y and

$\bar{\varepsilon}$ are in a quantitative agreement even when the calculated spectra themselves assort rather ill with the experimental ones. Surely, it is to keep in mind the uncertainties inherent in the experimental spectra we correlate our calculations with. It is to mention that the total neutron yield Y (1.15), as well as the mean energy $\bar{\varepsilon}$ (1.17), is just determined by the experimentally measured total photoabsorption cross-sections (1.11), (1.16), whereas the theoretical description of the photoneutron distributions (1.12), we put to use, is apparently model-dependent. Thereby some ambiguities might slip into the outcome, however plausible the underlying models were. Notwithstanding, our findings are relevant to describe the energy distribution of neutrons generated at the e-linac-based neutron sources, which is especially of value in lack of the appropriate reliable experimental measurements.

The neutron spectrum is of general scientific interest in its own right, and in certain applications it is essential to know its precise form. The generic findings of the presented study are intended to allow the optimal construction of the best-suited e-linac-based setups for the given experimental and industrial requirements.

Acknowledgements. The author is thankful to Z. Panteleev, A. Popov, P. Sedishev, Sh. Zainalov for valuable discussions.

REFERENCES

1. *Bockhoff K. H.* Properties of Neutron Sources // Proc. of Advisory Group Meeting on Properties of Neutron Sources, Leningrad, USSR, June 9–13, 1986. IAEA-TECDOC-410. Vienne, 1987. P. 35–55;
   Isotope Production and Application in the 21st Century // Proc. of the Third Intern. Conf. on Isotopes, Vancouver, Canada, Sept. 6–10, 1999. World Sci. Publ. Co. Inc. Vancouver, B. C. Stevenson, 2000.
2. *Gohar Y. et al.* Accelerator Driven Subcritical Assembly; Concept Development and Analyses. The RERTR-2004 Intern. Meeting. Vienna, 2004.
3. *Bunatian G. G., Nikolenko V. G., Popov A. B.* JINR Commun. E3-2010-144. Dubna, 2010.
4. *Akhiezer A. I., Berestetskii V. B.* Quantum Electrodynamics. M., 1959.
5. *Heitler W.* The Quantum Theory of Radiation. Oxford; London: Clarendon Press, 1954.
6. *Berestetskii V. B., Lifshits E. M., Pitaevskii L. P.* Relativistic Quantum Theory. Oxford: Pergamon, 1971.
7. *Shiff L. I.* // Phys. Rev. 1951. V. 83. P. 252.
8. *Bethe H., Heitler W.* // Proc. Roy. Soc. A. 1934. V. 146. P. 83.
9. The Nuclear Handbook / Ed. by O. R. Frisch. London: George Newnes Limited, 1958; The Tables of Physical Quantities / Ed. by I. K. Kikoin. M.: Atomizdat, 1976.
10. *Caldwell J. T. et al.* // Phys. Rev. C. 1980. V. 21. P. 1215;
    Veyssiere A. et al. // Nucl. Phys. A. 1973. V. 199. P. 45;

Arrudantro J. D. T. et al. // Phys. Rev. C. 1976. V. 14. P. 1499;
Ries H. et al. // Phys. Rev. C. 1984. V. 29. P. 2346.
11. *Bergere R., Beil H., Veyssiere A.* // Nucl. Phys. A. 1968. V. 121. P. 463;
Bramblett R. L. et al. // Phys. Rev. 1963. V. 120. P. 2723.
12. *Goryachev B. I. et al.* // Pis'ma ZhETF. 1968. V. 7. P. 210;
Ishkhanov B. S. et al. // J. Nucl. Phys. 1970. V. 12. P. 628;
Fuller E. G., Hayward E. // Nucl. Phys. 1962. V. 33. P. 431;
Veyssiere A. et al. // Nucl. Phys. A. 1970. V. 159. P. 561.
13. *Wilkinson D. H.* // Ann. Rev. Nucl. Sci. 1951. V. 9. P. 1;
Brown G. E., Bolsterli M. // Phys. Rev. Lett. 1959. V. 3. P. 472;
Kuchnir F. T. et al. // Phys. Rev. 1967. V. 161. P. 1236;
Griffin J. J. // Phys. Rev. Lett. 1966. V. 17. P. 478;
Rawlines J. et al. // Nucl. Phys. A. 1968. V. 122. P. 625.
14. *Blatt J. M., Weisskopf V. F.* Theoretical Nuclear Physics. N. Y.; London, 1952;
Berman B. L., Fultz S. C. // Rev. Mod. Phys. 1975. V. 47. P. 739.
15. *Veyssiere A. et al.* // Nucl. Phys. A. 1968. V. 121. P. 463;
Veyssiere A. et al. // Nucl. Phys. A. 1970. V. 159. P. 561.
16. *Barret R. F. et al.* // Nucl. Phys. A. 1973. V. 210. P. 355.
17. *Lui J. C. et al.* // Rad. Prot. Dosimetry. 1997. V. 70, No. 1–4. P. 49.
18. www-nds.IAEA.org (RIPL-2 (Level Density Segment)).
19. *Kuchnir F. T. et al.* // Phys. Rev. 1967. V. 161. P. 1236.
20. *Price G. A.* // Phys. Rev. 1953. V. 93. P. 1279.
21. *Katcoff S.* // Nucleonics. 1960. V. 18. P. 201;
Ziskin Yu. A., Lbov A. A., Sel'genkov L. I. Fission Products and Their Mass Distributions. M.: Gosatomizdat, 1963;
Gangrsky Yu. P., Markov B. N., Pereligin V. P. Fission Fragments Registration and Spectrometry. M.: Energoatomizdat, 1992.
22. The Nucl. Fis. Proc. / Ed. C. Wagemans. Boca Raton (FL): CRC Press, 1991.
23. *Levinger S.* // Phys. Lett. B. V. 82. P. 181;
Laget J. M. // Nucl. Phys. A. 1981. V. 358. P. 275c;
Ericson M., Rosa-Clot M. // Z. Phys. A. 1991. V. 324. P. 373;
Baumann B. et al. // Phys. Rev. C. 1988. V. 38. P. 1940;
Hayward E. // Phys. Rev. C. 1989. V. 40. P. 467.
24. *Lepretere A. et al.* // Nucl. Phys. A. 1987. V. 472. P. 533.
25. *Ryckbosch D., Carlos P., Lepretere A.* // Z. Phys. A. 1988. V. 329. P. 451.
26. *Lepretere A. et al.* // Nucl. Phys. A. 1981. V. 367. P. 237.
27. *Lepretre A. et al.* // Nucl. Phys. A. 1982. V. 390. P. 221.
28. *Lepretre A. et al.* // Ibid. P. 240.
29. *Blann M., Berman B. L., Komoto T. T.* // Phys. Rev. C. 1983. V. 28. P. 2286.
30. Nucl. Data Tables. 1971. V. 9, Nos. 4, 5.
31. *Audi G. et al.* // Nucl Phys. A. 2003. V. 729. P. 3;
Mandel D. G. // Nucl. Phys. A. 2006. V. 772. P. 113.
32. *Flaska M. et al.* // Nucl. Instr. Meth. A. 2005. V. 555. P. 329.
33. *Flaska M. et al.* // Nucl. Instr. Meth. A. 2004. V. 531. P. 392.

34. *Ene D. et al.* // Nucl. Instr. Meth. A. 2010. V. 618. P. 54.
35. *Flaska M. et al.* // Proc. of Enlar. Work. on NEMEA, Budapest, Nov. 5–8, 2003 / Ed. by A. J. M. Plompen. P. 103.
36. *Rochman D., Koning A. J., van der Marck S. C.* // Ann. Nucl. Eng. 2009. V. 36. P. 810; *Koning A. J., Duijvestijn M. C.* // Nucl. Phys. A. 2004. V. 744. P. 15.
37. *Kochler P. et al.* // Nucl. Phys. A. 1983. V. 294. P. 221.
Glendinning S. G. et al. // Nucl. Sci. Eng. 1982. V. 80. P. 256;
Handbook for Calculations of Nuclear Reactions Data. Ref. Input Parameters Library. IAEA-TECDOC-1034. 1998.
38. *Khokhlov Yu. A., Savin M. V.* // VI School on Neutron Physics, Alushta, USSR, Oct. 8–10, 1990. Dubna, 1991. P. 75.
39. *Burgart C. E. et al.* // Nucl. Sci. Eng. 1970. V. 42. P. 421;
Alsmiller R. G., Gabriel T. A., Guthrie M. P. // Nucl. Sci. Eng. 1970. V. 40. P. 365.
40. *Van Do Nguyen et al.* // J. Kor. Phys. Soc. 2006. V. 48. P. 382;
Kim G. N. et al. // Nucl. Instr. Meth. A. 2002. V. 485. P. 458.
41. *McCall R. C., Jenkins T. M., Shore R. A.* SLAC-PUB-2214. 1978;
McCall R. C., Swanson W. R. SLAC-PUB-2292. 1979.
42. *Swenson W. P.* IAEA TR. Tech. Rep. Ser. No. 188. Vienna: IAEA, 1979.
43. *Xu Hai-Bo et al.* // Chin. Phys. B. 2010. V. 19. P. 062901.
44. *Klug J. et al.* // Nucl. Instr. Meth. A. 2007. V. 577. P. 641.
45. *Altstadt E. et al.* // Ann. Nucl. Energy. 2007. V. 34. P. 36.
46. *Flaska M. et al.* // Nucl. Math. Comp. Sci.: A Century Anew, Gatlinburg, Tennessee, USA, Apr. 6–11, 2003. P. 1–11.
47. *Bo Nordell* // Nucl. Instr. Meth. 1984. V. 224. P. 547.
48. *Reda M. A., Harman G. F.* // Intern. Cent. for Dif. Data. 2004. V. 47. P. 212.
49. *Pronyae V. C. et al.* // Intern. Eval. of Neutron Cross-Sections Stan. IAEA Tech. Rep. 2006.
50. *Frohner F. H.* // Nucl. Sci. Eng. 1988. V. 103. P. 31.
51. *Ryves T.* // J. Phys. G. 1980. V. 6. P. 771;
Frehaut J. et al. // Nucl. Sci. Eng. 1980. V. 74. P. 29.